Computational Study of Li Ion Electrolytes Composed of Li_3AsS_4 Alloyed with Li_4GeS_4

Ahmad Al-Qawasmeh and N. A. W. Holzwarth*,z

Department of Physics, Wake Forest University, Winston-Salem, North Carolina 27109-7507, USA

First principles computational techniques are used to study properties of promising Li ion electrolytes, recently developed at Oak Ridge National Laboratory, based on alloys having the composition $Li_{3+x}As_{1-x}Ge_xS_4$. The crystal structure of pure Li_3AsS_4 is found to be characterized by the $Pmn2_1$ space group. Based on modifications of this structure, reasonable models of the $x = 1/4$ and $x = 1/3$ alloys are found to be in good agreement with the experimental X-ray diffraction patterns and to be consistent with the measured trends in Li ion conduction. As a consequence of their $Pmn2_1$-based structures, interstitial and interstitialcy mechanisms are found to be important for the Li ion conduction processes in these systems.
 [DOI: 10.1149/2.1131609jes]

Manuscript submitted May 25, 2016; revised manuscript received July 12, 2016. Published July 27, 2016.

The development of stable solid electrolytes with high ionic conductivity provides a challenge for basic materials research[1] which has been identified as a key to improved battery technologies.[2] Recent experimental studies by Sahu et al.[3] explored new electrolyte compositions for Li ion electrolytes and found promising results based on alloys of Li_3AsS_4 and Li_4GeS_4. Significantly higher ionic conductivity was found for the alloys $Li_{3+x}As_{1-x}Ge_xS_4$ with compositions $0 < x < 0.5$, compared with the pure materials, especially for $x = 1/3$. In order to understand the reported experimental results in terms of the stability and ion conduction mechanisms in this system, we have computationally examined this alloy system using first principles methods.

The notion of improving ionic conductivity by preparing solid solutions of two compatible ionic crystalline materials has been discussed several times in the literature. For example, in a 1977 publication, Hu et al.[4] studied a series of compounds with compositions $Li_{3+x}P_{1-x}Si_xO_4$, finding the highest conductivities for $x \approx 0.5$. This system has been further examined by several other researchers, including a recent combined experimental and simulation study by Deng et al.[5] who analyzed the detailed structures of the solid solutions in addition to the ionic conductivity from impedance and nuclear magnetic resonance measurements. For this system, in the composition range $0 \leq x \lesssim 0.5$, the compounds are derived from the structure of γ-Li_3PO_4, having the space group $Pnma$ (No. 62 as listed in the International Table of Crystallography[6]), with Si substituting for P. The simulation studies of this work suggest that the dominant Li ion migration mechanism for this system involves the correlated motions of interstitial and lattice Li ions in "interstitialcy" or "kick-out" processes.

Another related alloy system was recently investigated by Hori et al.[7] who determined the phase diagram of $Li_{3+x}P_{1-x}Ge_xS_4$. These authors find that for very small values of x ($0 \leq x \leq 0.02$), the system takes the $Pmn2_1$ (No. 31) structure of γ-Li_3PS_4, but for $0.02 \leq x < 0.2$ the system takes the $Pnma$ (No. 62) structure of β-Li_3PS_4. The alloy system having the β-Li_3PS_4 structure was found to have a room temperature ion conductivity of 10^{-3} S/cm for $x = 0.2$.[8] For larger values of x the system includes the so-called superionic conducting phase[9] for $x = 1/3$ which is usually written as $Li_{10}GeP_2S_{12}$ (LGPS). The LGPS structure is found for values of $0.2 < x < 0.6$, while for $x > 0.6$ the system takes the $Pnma$ structure of Li_4GeS_4. From the temperature dependence of the phase diagram, the authors argue that these structures are stabilized by entropy which is effected by the distribution of differently sized building blocks of PS_4 and GeS_4 ions. The LGPS system has been shown[9,10] to have a room temperature Li ion conductivity of 10^{-2} S/cm.

The importance of the lattice structure in determining the ionic conductivity of these electrolytes was recently shown by Liu et al.[11] who developed a novel preparation method which stabilizes the β-Li_3PS_4 structure at room temperature and increases the ionic conductivity by a factor of 100 to 10^{-4} S/cm. Other preparation methods have found[8,12] that pure β-Li_3PS_4 is not stable at room temperature, but its high temperature Li ion conductivity extrapolated to room temperature is approximately 10^{-6} S/cm.

For the $Li_{3+x}As_{1-x}Ge_xS_4$ alloy system studied by Sahu et al.,[3] which is the subject the present computational study, the X-ray experimental results suggest that the structure remains that of the Li_3AsS_4 lattice throughout the composition range $0 \leq x \leq 0.5$. While a more detailed analysis of the X-ray patterns may reveal some structural variations, we based our simulations on the assumption that Ge substitutes for As in the Li_3AsS_4 structure. The first task of the simulations is to determine the Li_3AsS_4 structure itself. Secondly, the likely Ge substitutions and their corresponding placements of the extra Li sites must be determined. Once plausible structures for the alloy are determined, the ion migration mechanisms can be investigated for each structure.

Computational Methods

The computational methods used in this work are based on density functional theory (DFT),[13,14] using the projected augmented wave (PAW)[15] formalism. The PAW basis and projector functions were generated by the ATOMPAW[16] code and used in QUANTUM ESPRESSO[17] package. Visualizations were constructed using the *XCrySDEN*,[18,19] *VESTA*[20] software packages.

The exchange correlation function is approximated using the local-density approximation (LDA).[21] The choice of LDA functional was made based on previous investigations[22–30] of similar materials which showed that provided that the lattice constants are scaled by a correction factor or 1.02, the simulations are in good agreement with experiment, especially lattice vibrational frequencies and heats of formation.

In this work, the heat of formation ΔH_f reported here is determined at 0 degrees K as estimated from the total electronic energy of the material per formula unit minus the energies of the elemental constituents in their standard states as defined by the CRC Handbook.[31] For example, the heat of formation for the alloy can be approximated from the zero temperature total energy results according to

$$\Delta H_f = E[Li_{3+x}As_{1-x}Ge_xS_4] - (3+x)E_{\rm std}(Li) - (1-x)E_{\rm std}[As] - xE_{\rm std}[Ge] - 4E_{\rm std}[S], \quad [1]$$

where $E_{\rm std}$ corresponds to the total energies of Li in the bcc structure, As in the $R\bar{3}m$ structure, Ge in the diamond structure, and S in the $Fddd$ ($\alpha - S_8$) structure, respectively. Also of interest is the decomposition energy (ΔH_D) for an alloy which can also be estimated from

*Electrochemical Society Member.
zE-mail: natalie@wfu.edu

the zero temperature total energy results according to:

$$\Delta H_D = E[Li_{3+x}As_{1-x}Ge_xS_4] - (1-x)E[Li_3AsS_4] - xE[Li_4GeS_4]. \quad [2]$$

With this sign convention, a negative value for ΔH_D implies that the alloy is stable with respect to decomposition into the pure materials. These energy estimates neglect the effects of finite temperature and pressure which van de Walle and Ceder[32] estimate to contribute 10^{-2} eV/atom at room temperature for most materials.

For analyzing the heats of formation and other perfect crystal properties, calculations were performed with plane wave expansions of the wave function including $|\mathbf{k}+\mathbf{G}|^2 \leq 64$ bohr^{-2} and with a Brillouin-zone sampling grid density of at least 10^{-3} bohr^{-3}/**k** point. The partial densities of states were calculated as described in previous work,[26,29] using weighting factors based on the charge within the augmentation spheres of each atom with radii $r_c^{Li} = 1.6$, $r_c^{As} = 2.3$, $r_c^{Ge} = 2.1$, and $r_c^{S} = 1.7$ in bohr units. The reported partial densities of states curves $\langle N^a(E)\rangle$ were averaged over the atomic sites of each type a.

Li vacancies and interstitials were modeled in supercell containing 16, 16, and 24 formula units for simulating pure Li_3AsS_4, the alloy $Li_{13/4}$ $As_{3/4}$ $Ge_{1/4}S_4$, and the alloy $Li_{10/3}As_{2/3}$ $Ge_{1/3}$ S_4, respectively. For the case of $Li_{10/3}As_{2/3}$ $Ge_{1/3}$ S_4, the plane wave cut off was reduced to 49 bohr^{-2}. The estimated error for the relative energies computed with the reduced plane wave cutoff is less than 0.02 eV. These supercells were used to estimate the minimum energy path for Li ion migration using the "nudged elastic band" (NEB) method[33–35] as programmed in the QUANTUM ESPRESSO package, using 5 images between each metastable configuration. In modeling charged defects (Li ion vacancies or interstitials), the system was assumed to remain electrically insulating and a uniform background charge was added in order to evaluate the electrostatic interactions. For each minimum energy path, the migration energy, E_m was determined as the energy difference between the lowest and highest energy of the path. The "formation energies" E_f for producing neutral defects in the form of vacancy-interstitial pairs were calculated for the same supercells. These energies are related to the experimentally measured ionic conductivity through an Arrhenius relationship of the form

$$\sigma = \frac{A}{T} e^{-E_A/kT}, \quad [3]$$

where A denotes a constant, T denotes the temperature in Kelvin, k denotes the Boltzmann constant, and E_A denotes the activation energy for ion migration. The activation energy is related to the migration and formation energies according to[36]

$$E_m + \tfrac{1}{2}E_f \geq E_A \geq E_m. \quad [4]$$

In Eq. 4 the upper limit of E_A applies to the "intrinsic" case when ion migration must be preceded by the creation of a pair of vacancy and interstitial ions by thermal activation. The lower limit applies to the "extrinsic" case when a population of vacancy or interstitial ions is available so that the conduction depends only the thermal activation due to the migration energy barriers characterized by E_m. In principle, the energy of charged defects should be corrected for finite size errors by using one of several methods reported in the literature.[37,38] This was not done in the present work, although we expect that the finite size errors for energy difference such as E_m benefit from error cancellation.

Results

Structures of the pure materials.—To the best of our knowledge, the crystal structure of Li_3AsS_4 has not been analyzed, although its X-ray diffraction pattern is reported by Sahu et al.[3] It is reasonable to assume that Li_3AsS_4 has structural properties similar to those of Li_3PS_4, which has been well studied.[12,26,39–42] As mentioned in the introduction, Li_3PS_4 is known to have the low temperature structure, γ-Li_3PS_4, characterized by the space group $Pmn2_1$ (No. 31). At temperatures between 200 and 300 degrees C, a transition to the β-Li_3PS_4 structure has been reported,[12,41] which is characterized by the space group *Pnma* (No. 62) with fractional occupancy of some of the Li sites. The β-Li_3PS_4 structure can be stabilized at room temperature and has been shown to have higher Li ion conductivity than the γ phase.[40] In previous work, we simulated the ideal crystalline structures of four models of Li_3PS_4 based on the ordered structures of $Pmn2_1$ γ-Li_3PS_4, *Pnma* γ-Li_3PO_4, and two idealizations of disordered *Pnma* β-Li_3PS_4.[26] The idealizations of disordered *Pnma* β-Li_3PS_4 were labeled β-Li_3PS_4-*b* and β-Li_3PS_4-*c* representing models with 100% occupancy of the Li sites with Wyckoff labels *b* and *c*, respectively. More recently, Ganesh et al.[39] have shown that the disordered β-Li_3PS_4 structure can be explained by using molecular dynamics (MD) simulations which show that the 70% occupancy of the *b* site and 30% occupancy of the *c* site correlates with the site analysis of the time averaged Li MD trajectories.

Table I. Heats of formation (in eV), as defined in Eq. 1, for Li_3AsS_4 and Li_3PS_4 in four different model structures.

Structure	Li_3AsS_4 ΔH_f (eV)	Li_3PS_4 ΔH_f (eV)
γ-Li_3PS_4 ($Pmn2_1$)	−7.17	−8.37
γ-Li_3PO_4 (*Pnma*)	−6.95	−8.18
β-Li_3PS_4-*b* (*Pnma*)	−7.00	−8.28
β-Li_3PS_4-*c* (*Pnma*)	−7.03	−8.25

Table I lists the heats of formation (ΔH_f) calculated for four structural models structures of Li_3AsS_4 and Li_3PS_4. The heat of of formation results given in Table I, indicate that the ground state structure of Li_3AsS_4 corresponds to the $Pmn2_1$ ground state structure of γ-Li_3PS_4. The calculated lattice constants are $a = 7.65$ Å, $b = 6.54$ Å, $c = 6.14$ Å, which agrees well with experiment when scaled by the 1.02 LDA correction factor. A structural diagram of Li_3AsS_4 in this structure is shown in Fig. 1. The calculated fractional coordinates are listed in Table AI in the Appendix.

In order to compare the simulation results with experiment, we generated the X-ray powder diffraction pattern with the help of the Mercury[43] software package and compared it with the experimental pattern, obtained by digitizing the published results,[3] as shown in Fig. 2. The simulated powder pattern is seen to be in good agreement with the experimental results. Also included in Fig. 2 is the

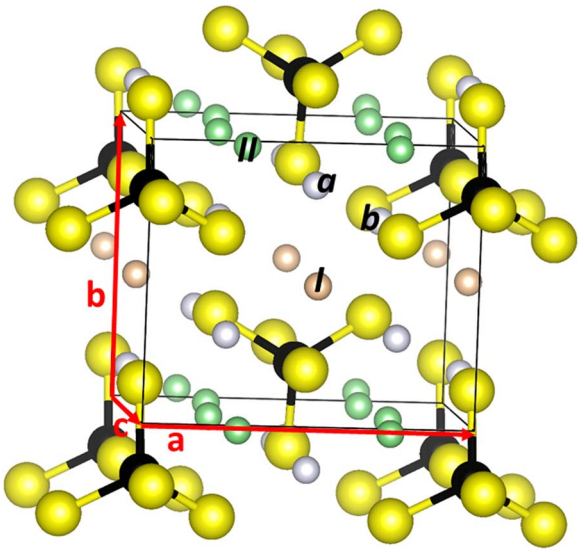

Figure 1. Ball and stick diagram of the unit cell of the $Pmn2_1$ structure of Li_3AsS_4. The Li, As and S sites are displayed with gray, black, and yellow balls respectively. The labels *a* and *b* indicate examples of Li sites with those Wyckoff labels. Also indicated are the lowest energy interstitial sites for Li ions, labeled *I* and *II* and tinted orange and green respectively.

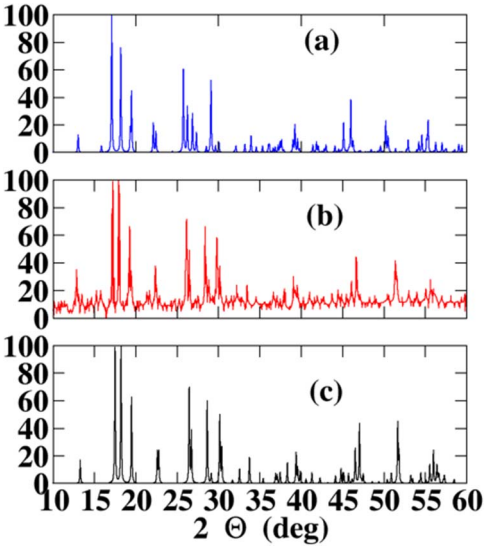

Figure 2. Comparison of X-ray powder diffraction patterns from simulations and experiment. Panel (b) shows the experimental data from Ref. 3, plotted from a digitized analysis of the published graph. Panels (c) and (a) show the powder diffraction patterns generated using Mercury[43] software from the simulation results of the $Pmn2_1$ γ-Li_3PS_4 and *Pnma* β-Li_3PS_4-*c* structures, respectively. For both of the simulations, the 1.02 LDA scaling correction was applied.

simulated powder pattern for the so-called β-Li_3PS_4-*c* model structure of Li_3AsS_4, which has less favorable correspondence to the experimental pattern, consistent with its calculated total energy being 0.14 eV above that of the ground state configuration.

From the simulation results and from the reported X-ray diffraction experiments on Li_3PS_4 and its alloys,[44] it is reasonable to assume that the $Pmn2_1$ structure forms the basis of the structure throughout the composition range. That is, unlike Li_3PS_4, there is no evidence of multiple structural phases.

In anticipation of the analysis of Li ion migration in this material, it is useful to study the relative energies of vacancy and interstitial defects. The $Pmn2_1$ structure of Li_3AsS_4 has two geometrically distinct host lattice sites with Wyckoff labels *a* and *b* as indicated in Fig. 1. We found several metastable interstitial sites in the lattice; the lowest energy sites are labeled *I* (having a multiplicity of 2 in the conventional unit cell) and *II* (having a multiplicity of 4). These sites and their equivalents are shown in Fig. 1. The relative energies of vacancies in the 16 formula unit supercell are given in Table II. Interestingly, the relative energies and fractional coordinates of the vacancy and interstitial sites are calculated to be very similar for Li_3AsS_4 and its γ-Li_3PS_4 analog.

The crystal structure of Li_4GeS_4, which has been studied by several groups,[45–47] has the *Pnma* (No. 62) space group. The calculated lattice constants are $a = 13.83$ Å, $b = 7.59$ Å, and $c = 6.00$ Å, in good agreement with the literature results after scaling by 1.02 to correct for the systematic LDA error. The local configuration of the GeS_4 tetrahedra of this structure are very similar to those of AsS_4, consistent with the formation of substitutional alloys.

Table II. List of relative energies Δ*E* (eV) for vacancy (Vac) and interstitial (Inter) Li sites in Li_3AsS_4 compared with the corresponding defects in γ-Li_3PS_4 calculated for 2 × 2 × 2 supercell models. The zero energies are taken to be the *b* site for the vacancy defect and the *I* site for the interstitial defect. The "Position" entries indicate the fractional coordinates referenced to the conventional cell of the perfect lattice.

		Li_3AsS_4		γ-Li_3PS_4	
Type	Label	Position	Δ*E*	Position	Δ*E*
Vac	*a*	(0.00, 0.85, 0.99)	0.07	(0.00, 0.82, 1.00)	0.05
Vac	*b*	(0.24, 0.32, 0.00)	0	(0.24, 0.32, 0.00)	0
Inter	*I*	(0.00, 0.49, 0.65)	0	(0.00, 0.48, 0.64)	0
Inter	*II*	(0.23, 0.00, 0.68)	0.09	(0.24, 0.00, 0.66)	0.00

Structures of the alloys.—In order to perform detailed first principles simulations of the alloy structures, it is necessary to find plausible ordered structures within computationally manageable supercells as described below. We also briefly investigated the question of whether the material produced in the experiment is likely to be an ordered structure such as found in our simulations, or more likely to be a disordered alloy with Ge replacing As randomly. In the X-ray power diffraction patterns, the ordered structures are characterized by site occupancy factors of 1, while disordered structures have fractional site occupancies representing incoherent averages of diffractions from all possible crystal configurations. Using the Mercury software[43] to generate simulated X-ray powder patterns, it is possible to adjust the occupancy factors to compare the patterns for the ordered structures with those generated for corresponding structures with random occupation of the Ge and As sites. The simulations show small differences in the X-ray patterns. While it is possible that future experiments could detect such differences, the reported experimental powder patterns[3] are in good agreement with the generated X-ray powder patterns of the ordered structures and nearly equally good agreement with the corresponding patterns generated for the disordered structures. This suggests that the structures discussed below are very plausible models, but not the only possibilities.

The search for optimal alloy structures was based on supercells of the Li_3AsS_4 structure; four and six formula unit supercells were used for the $x = 1/4$ and $x = 1/3$ alloys respectively. For each supercell, all unique configurations of Ge substitutions were considered. For each Ge substitution an additional Li was added at a grid of likely positions. QUANTUM ESPRESSO[17] was used to optimize the structures of each of the initial configurations. For each alloy concentration considered, the optimized alloy model was found to have the lowest energy of the configurations considered by 0.2–0.3 eV.

In order to check for additional alloy models, we also sampled a few configurations from larger supercells with the help of symmetry analysis available from Site Occupancy Disorder (SOD) program of Grau-Crespo et al.[48] Although we failed to find alloy structures with lower energy, it is possible that a more exhaustive search may reveal additional possibilities. On the other hand, the alloy models that we did find, appear to make optimal use of the original Li_3AsS_4 structure and its low energy interstitial sites, as explained in more detail below.

3/4 Li_3AsS_4 + 1/4 Li_4GeS_4.—One of the alloys studied by Sahu et al.[3] is composed of Li_3AsS_4 and Li_4GeS_4 in the ratio 3:1, forming the compound $Li_{13/4}As_{3/4}Ge_{1/4}S_4$. The optimal model structure for this alloy is shown in Fig. 3a. It can be described in terms of a 2 × 1 × 1 supercell of the $Pmn2_1$ structure of Li_3AsS_4, with Ge substituting for As in the $x = 0$ plane and the associated extra Li located close by as indicated with the symbol "*x*" in the figure. The *x* site Li of the alloy occupies a position close to interstitial site of type "*I*" of the original Li_3AsS_4 lattice. This structure is 0.15 eV lower in energy than the other configurations we investigated for this alloy. The optimized lattice constants of this structure are $a = 15.20$ Å, $b = 6.60$ Å, and $c = 6.13$ Å, corresponding to a very slight contraction of the Li_3AsS_4 host lattice along the *a* axis. The structure shown in Fig. 3a has the space group *Pm* (No. 6). The fractional coordinates of the unique atoms are listed in the Appendix in Table AII.

In anticipation of the analysis of Li ion migration in this material, we studied the relative energies of vacancy and interstitial defects. The *Pm* structure of the 1/4 alloy has 8 distinct Li sites and 6 distinct interstitial sites as shown in Fig. 3a. The corresponding relative vacancy and interstitial energies are listed in Table III. From the simulations based on 16 formula unit supercells, the *x* site Li ion has the lowest vacancy energy, defined as $\Delta E = 0$. The nearest neighbor

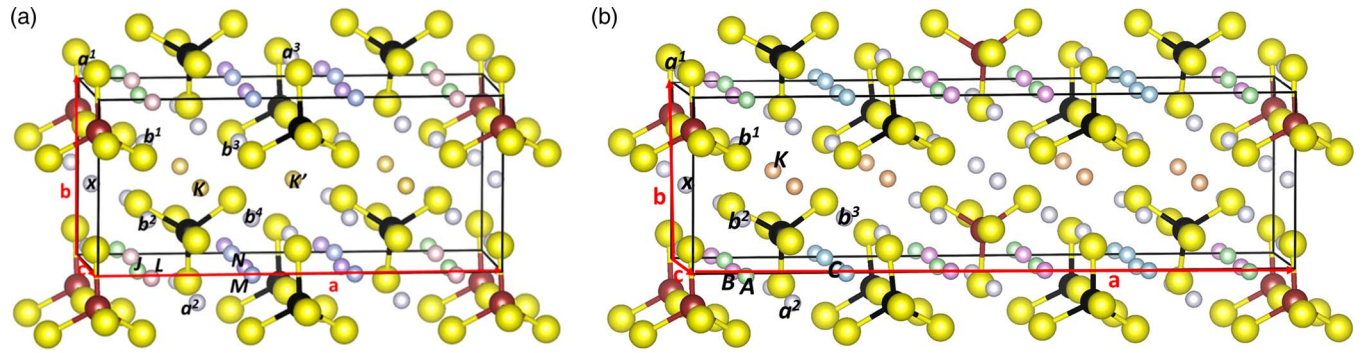

Figure 3. Ball and stick model of the optimized structures of the $Li_{3+x}As_{1-x}Ge_xS_4$ alloys considered in this study. The Li, As, Ge, and S atomic sites are shown in gray, black, dark red, and yellow respectively. The labels a^i and b^i for $i = 1, 2, ...$ represent Li sites corresponding the the a and b Wyckoff labels of pure Li_3AsS_4, which are now modified in these alloys. The label x references the additional Li site introduced by the presence of Ge. Also shown are the low energy interstitial sites for Li ions. (a) Shows the alloy $x = 1/4$ with interstitial sites indicated with green, pink, purple, blue, orange, and orange tint corresponding to the unique labels, J, L, M, N, K, and K', respectively. (b) Shows the alloy $x = 1/3$ with interstitial sites indicated with green, pink, blue, and orange tint corresponding to the unique labels A, B, C, and K, respectively.

Li vacancy sites, a^1, b^1, and b^2, are all unstable relative to the x site vacancy. These are listed in Table III with $\Delta E = 0$ because their relaxed configuration is that of x site vacancy. The vacancy energies for Li ions further from the Ge site are more than 0.5 eV higher in energy. Accordingly, we expect that the population of vacancies on the a^2, a^3, b^3, and b^4 sites to be substantial lower than the population of vacancies on the x sites. However, entropy effects[32] which reduce the free energies, increase the probability of forming these vacancies.

The interstitial energies of sites K and K', both corresponding to the type I interstitial of the pure Li_3AsS_4 lattice, are 0.06 eV higher in energy than the lowest energy J interstitial site, which is defined as $\Delta E = 0$. The four unique interstitial sites J, L, M, and N all correspond to the the type II interstitials in pure Li_3AsS_4. The lowest energy J site is closest to the plane containing the substitutional Ge atoms, although because of its c axis placement, the interstitial L site interstitial is closer to its nearest Ge site, as noted in Table III.

2/3 Li_3AsS_4 + 1/3 Li_4GeS_4.—Another alloy studied by Sahu et al.,[3] is composed of Li_3AsS_4 and Li_4GeS_4 in the ratio 2:1, forming the compound $Li_{10/3}As_{2/3}Ge_{1/3}S_4$. The optimal model structure for this alloy is shown in Fig. 3b. It can be described in terms of a $3 \times 1 \times 1$ supercell of pure Li_3AsS_4, with Ge substituting for As in planes perpendicular to the **a**-axis at the fractional coordinates $x = 0$ and $x = 1/2$. The associated 2 extra Li sites are located close by as indicated with the symbols x in the figure. The x site Li's of the alloy occupy positions close to interstitial site of type "I" of the original Li_3AsS_4 lattice. This structure is 0.27 eV lower in energy than all the other configurations we investigated for this alloy. The lattice constants of this optimized structure are $a = 22.77$ Å, $b = 6.60$ Å, and $c = 6.14$ Å, corresponding to a slight contraction of the Li_3AsS_4 lattice along the a axis. This structure of the $Li_{10/3}As_{2/3}Ge_{1/3}S_4$ alloy has the space group $Pmn2_1$ (No. 31), as does the optimal structure of the Li_3AsS_4 host lattice. The fractional coordinates of the unique atoms are listed in the Appendix in Table AIII.

In anticipation of the analysis of Li ion migration in this material, we studied the relative energies of vacancy and interstitial defects. The $Pmn2_1$ structure of the 1/3 alloy has 6 distinct Li sites and 4 distinct interstitial sites as shown in Fig. 3b. The corresponding relative vacancy and interstitial energies are listed in Table IV. From the simulations based on 24 formula unit supercells, the x site Li ion has the lowest vacancy energy, defined as $\Delta E = 0$. As in the case of the 1/4 alloy, the nearest neighbor Li vacancy sites, a^1, b^1, and b^2, are all unstable relative to the x site vacancy. Vacancies at sites further from the Ge substitutions, a^2 and b^3 are approximately 0.5 eV

Table III. List of relative energies ΔE (eV) for vacancy (Vac) and interstitial (Inter) Li sites in $Li_{13/4}$ $As_{3/4}$ $Ge_{1/4}S_4$ based on 16 formula unit simulations. For each defect site, the column labeled "Ref" lists the equivalent site in the pure Li_3AsS_4 structure. The column labeled "Proximity" indicates the distance of the defect to the nearest Ge (in Å). For the vacancy sites, the '*' indicates that the vacancy is unstable with respect to neighboring x site vacancy (defined as the 0 energy). For the interstitial sites, the lowest energy interstitial energy (J) was defined as zero.

Type	Label	Ref	Proximity (Å)	ΔE (eV)
Vac	a^1*	a	3.6	0.00
Vac	b^1*	b	3.7	0.00
Vac	a^2	a	3.8	0.65
Vac	b^2*	b	3.8	0.01
Vac	a^3	a	8.5	0.61
Vac	b^3	b	6.5	0.56
Vac	b^4	b	6.6	0.54
Vac	x	I	3.0	0.00
Int	K	I	4.3	0.06
Int	K'	I	8.8	0.06
Int	J	II	2.9	0.00
Int	L	II	2.6	0.07
Int	M	II	5.8	0.12
Int	N	II	7.2	0.13

Table IV. List of relative energies ΔE (eV) for vacancy (Vac) and interstitial (Inter) Li sites in $Li_{10/3}$ $As_{2/3}$ $Ge_{1/3}S_4$ based on 24 formula unit simulations. For each defect, the column labeled "Ref" lists the equivalent site in the pure Li_3AsS_4 structure. The column labeled "Proximity" indicates the distance of the defect to the closest Ge (in Å). For the vacancy sites, the '*' indicates that the vacancy is unstable with respect to neighboring x site vacancy (defined as the 0 energy). For the interstitial sites, the lowest energy interstitial energy (B) was defined as zero.

Type	Label	Ref	Proximity (Å)	ΔE (eV)
Vac	a^1*	a	3.6	0.00
Vac	b^1*	b	3.7	0.00
Vac	a^2	a	3.8	0.59
Vac	b^2*	b	3.8	0.00
Vac	b^3	b	6.5	0.49
Vac	x	I	3.0	0.00
Int	K	I	4.3	0.07
Int	A	II	2.6	0.05
Int	B	II	2.9	0.00
Int	C	II	6.0	0.14

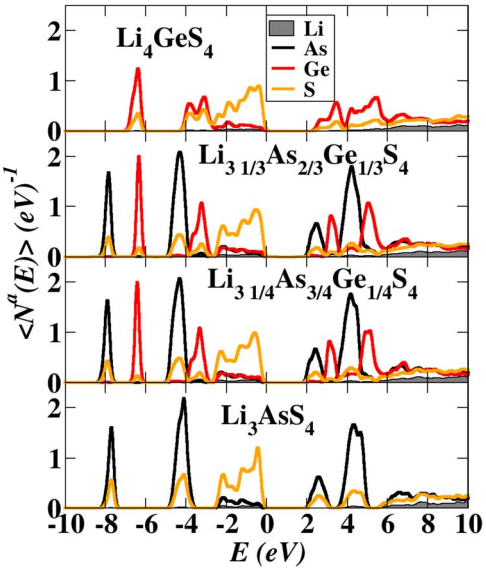

Figure 4. Partial densities of states plots for the pure materials Li_4GeS_4 and Li_3AsS_4 in their ground state structures and for the two alloys $Li_{3+x}As_{1-x}Ge_xS_4$ with $x = 1/4$ and $x = 1/3$, in their optimized structures.

Table V. Heats of formation (ΔH_f) and of decomposition (ΔH_D) (in eV/formula unit) for pure and alloy materials.

	ΔH_f	ΔH_D
Li_3AsS_4	−7.17	
Li_4GeS_4	−10.18	
$Li_{13/4}As_{3/4}Ge_{1/4}S_4$	−7.86	0.06
$Li_{10/3}As_{2/3}Ge_{1/3}S_4$	−8.09	0.06

or higher in energy. As in the case of the 1/4 alloy, we expect that entropy effects will enable the population of vacancies on these to be non negligible. The interstitial sites have relative energies similar to those of the 1/4 alloy. In this case, the lowest energy site is labeled B, defined as $\Delta E = 0$, and has the smallest distance from the plane containing the Ge substitutions.

Densities of states and heats of formation.—The partial density of states analysis provides qualitative information about the atomic contributions to the occupied and unoccupied states of the materials. Fig. 4 shows the results for the materials in this study. It is interesting that the two alloys with $x = 1/4$ and $x = 1/3$ show nearly identical densities of states. The valence band of these materials is primarily composed of the S $3p$ states, while the conduction bands are composed of unoccupied As and Ge states, hybridized with S. In general the states associated with Ge lie above their corresponding As counter parts; the bandgap of the alloy is expected to be similar to that of Li_3AsS_4.

A more quantitative measure of density functional results is the heats of formation (ΔH_f) of the materials referenced to the elemental materials in their standard states determined from the total energies of the systems as described by Eq. 1. Also of interest is the decomposition energies (ΔH_D) for the alloys which can also be estimated from the zero temperature total energy results according to Eq. 2. Both of these energies are listed in Table V. The results show that that Li_4GeS_4 has the largest magnitude of ΔH_f of the materials studied. Small positive values of ΔH_D having the order of magnitude of the expected finite temperature and pressure corrections,[32] suggest that at equilibrium the alloys are marginally stable with respect to decomposition into the pure materials.

Ion migration mechanisms.—Using the NEB technique described in the Computational methods section, we examined several possible Li ion migration processes in Li_3AsS_4 and in the $Li_{3+x}As_{1-x}Ge_xS_4$ alloys. The results are summarized in Table VI and the details are described below.

Ion Migration in pure Li_3AsS_4.—For defect-free crystalline materials, the energy to form an interstitial vacancy pair, E_f contributes to the activation energy for conductivity as described in Eq. 4. For pure Li_3AsS_4, we found the lowest formation energy for an interstitial-vacancy pair to be $E_f = 0.86$ eV corresponding to a type I interstitial site and a nearby b vacancy site. The formation energy for a type II interstitial and nearby b vacancy is very similar. The corresponding interstitial-vacancy pair formation energy in γ-Li_3PS_4 is $E_f = 0.81$ eV due to a type II interstitial site being occupied by a nearby b vacancy site.[26]

Several Li ion vacancy migration paths in Li_3AsS_4 were investigated according to the diagram shown in Fig. 5a with the resulting NEB energies shown in Fig. 5b. For comparison, the corresponding NEB energies for γ-Li_3PS_4 are also shown in Fig. 5b. For these paths, the energies for Li vacancy migration in Li_3AsS_4 are considerably higher than that of the thiophosphate. The migration energies E_m are determined as the maximum energy difference along the path which is $E_m = 0.4$ eV for Li_3AsS_4 and $E_m = 0.3$ eV for γ-Li_3PS_4.

Because of the relatively large value of E_m for pure Li ion vacancy migration in Li_3AsS_4, we were motivated to investigate other diffusion mechanisms such as ion migration involving interstitial Li ion sites. Three different such paths were found as shown in Fig. 6. Two paths with net motion along the **b** axis are shown in Fig. 6a. The path indicated by red arrows $II_1 \rightarrow I_1 \rightarrow II_4$ corresponds to pure interstitial migration. The path indicated by black arrows involves a kick-out process of the II_1 interstitial ion displacing an "a" host lattice ion into the I_1 interstitial position. Subsequently, the I_1 interstitial Li ion displaces the "b" host lattice ion into the II_4 interstitial position. The third path, with net motion along the **c** axis, is shown

Table VI. Summary of calculated optimal Li ion migration energies E_m and interstitial-vacancy pair formation energies E_f, compared with experimental activation energies E_A quoted or analyzed from Ref. 12 for γ-Li_3PS_4 and from Ref. 3 for $Li_{3+x}As_{1-x}Ge_xS_4$. All energies are in eV units.

		Simulation			Experiment
Material	Migration Path	E_m	E_f	$E_m + \frac{1}{2}E_f$	E_A
γ-Li_3PS_4	Vacancy along **a** axis	0.3	0.8	0.7	0.5
Li_3AsS_4	Vacancy along **a** or **c** axes	0.4	0.9	0.8	0.4
Li_3AsS_4	Interstitial along **c** axis	0.3	0.9	0.7	0.4
Li_3AsS_4	Interstitial along **b** axis	0.5	0.9	0.9	0.4
Li_3AsS_4	Kick-out along **b** axis	0.3	0.9	0.8	0.4
$Li_{13/4}$ $As_{3/4}$ $Ge_{1/4}S_4$	Kick-out along **b** axis	0.3	0.3	0.4	0.3
$Li_{13/4}$ $As_{3/4}$ $Ge_{1/4}S_4$	Interstitial along **c** axis	0.3	0.3	0.4	0.3
$Li_{10/3}As_{2/3}Ge_{1/3}S_4$	Kick-out along **b** axis	0.2	0.3	0.4	0.2
$Li_{10/3}As_{2/3}Ge_{1/3}S_4$	Interstitial along **c** axis	0.2	0.3	0.3	0.2

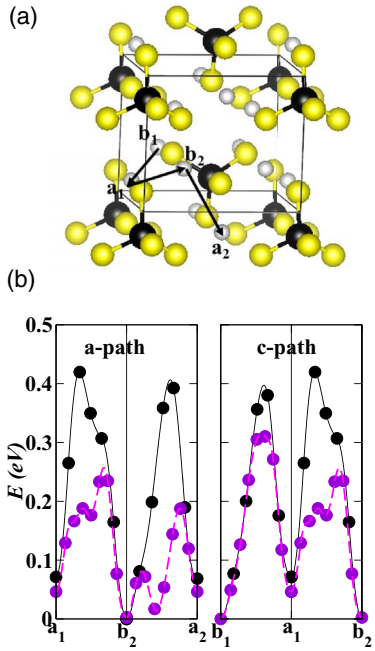

Figure 5. (a) Ball and stick model of Li_3AsS_4 indicating Li ion vacancy migration pathways. (b) Corresponding minimum energy paths for Li ion vacancy migration along the **a** and **c** axes. In addition to the results for Li_3AsS_4, the corresponding NEB migration energies are also given for γ-Li_3PS_4 as indicated with purple symbols and lines.

in Fig. 6b. This is a purely interstitial migration between neighboring II type interstitials between sites $II_1 \rightarrow II_2 \rightarrow II_3$. For this path, the NEB analysis shows a correlated motion of the host lattice Li ion at the neighboring "a" site was found in partial kick-out like process. While this correlated motion contributes to the energetics of the process, it does not seem to directly contribute to ion migration. The corresponding minimum energy paths as determined from the NEB method are shown in Fig. 7. We see that for the paths along the **b** axis, the kick-out mechanism, with a migration energy $E_m = 0.34$ eV, is more favorable than the pure interstitial mechanism with a migration energy $E_m = 0.5$ eV, and also more favorable than the pure vacancy migration shown in Fig. 5. The pure interstitial migration path along the **c** axis has a migration energy E_m=0.31 eV, which is the most favorable of the paths considered for this material.

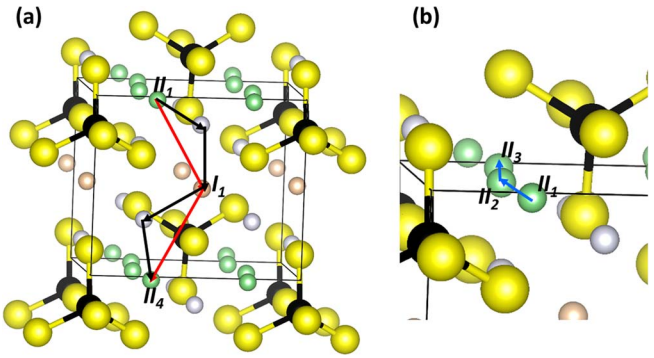

Figure 6. Ball and stick diagram of Li_3AsS_4 using the same orientation and ball convention as Fig. 1. (a) Indicates a migration path with net motion along the **b** axis, the red arrows indicating the pure interstitial process and the black arrow indicating a related process including the "kick-out" of host lattice ions at each step. (b) Indicates a migration path with net motion along the **c** axis with a pure interstitial process.

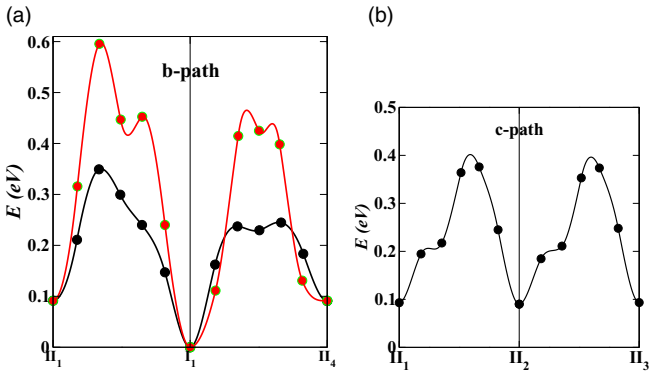

Figure 7. (a) Minimum energy paths as determined from the NEB method for the pure interstitial mechanism along the **b** axis (red curve) and for the kick-out mechanism (black curve) corresponding to the diagram in Fig. 6a. (b) Minimum energy path as determined by the NEB method for the pure interstitial mechanism along the **c** axis corresponding to the diagram in Fig. 6b.

Ion migration in $Li_{13/4}$ $As_{3/4}$ $Ge_{1/4}S_4$.—For an alloy, it is expected that the role of the interstitial-vacancy pair formation energy E_f in contributing to the activation energy as described by Eq. 4 is less important than it is in highly ordered crystals. However, E_f is a well-defined quantity within our ordered models for these alloys. For the $Li_{13/4}$ $As_{3/4}$ $Ge_{1/4}S_4$ alloy, the lowest formation energy was found to be $E_f = 0.27$ eV involving the J type interstitial and its neighboring "x" site vacancy. This value of E_f is considerably smaller than that pure Li_3AsS_4 and its mechanism is a consequence of the extra "x" Li ions introduced by Ge.

For several reasons, it is reasonable to assume that interstitial and interstitiacy ion migration mechanisms, and not pure vacancy mechanisms, are of main importance for ion migration in Li_{3+x} As_{1-x} Ge_xS_4 alloys. Firstly, as discussed for pure Li_3AsS_4, these mechanisms have smaller migration energy barriers in the Li_3AsS_4 lattice itself. Secondly, as discussed above, the x site Li can contribute to the interstitial population with a relatively small formation energy. Finally, as discussed in the structural analysis section, several potential Li ion vacancy sites in the vicinity of Ge (sites a^1, b^1, and b^2 shown in Fig. 3a) are found to be unstable relative to the x site vacancy, limiting the pure vacancy pathways available within this lattice.

As discussed above, for pure Li_3AsS_4, the most energetically favorable Li ion migration paths were found to be a kick-out mechanism along **b** axis and a pure interstitial mechanism along the **c** axis. In the $Li_{13/4}$ $As_{3/4}$ $Ge_{1/4}S_4$ alloy, several variations of these paths occur; it is expected that their energy profiles will depend on the location of the paths relative to the planes of Ge substitution.

We studied three representative paths based on a kick-out mechanism with net migration along the **b** axis, as shown in Fig. 8a. The path $L_1 \rightarrow b^2 \rightarrow K_2' \rightarrow a^2 \rightarrow L_2$ has a migration energy of $E_m = 0.28$ eV. It is geometrically equivalent to the path $II_4 \rightarrow b \rightarrow I_1 \rightarrow a \rightarrow II_1$ with a migration energy of $E_m = 0.34$ eV found in the pure Li_3AsS_4 structure. A contributing factor to the decrease in E_m for this path in the alloy is the alignment of the interstitial energies of the L and K' sites due to their proximity to Ge as reported in Table III. A similar path within the 1/4 alloy is represented by the sequence $N_1 \rightarrow a^3 \rightarrow K_1 \rightarrow b^3 \rightarrow N_2$ which is found to have a migration energy of $E_m = 0.31$ eV, involving sites further from the Ge substitutions. We also considered the path represented with the sequence $J_1 \rightarrow a^2 \rightarrow K_1' \rightarrow b^2 \rightarrow J_2$. As illustrated in Fig. 9a, the migration energy for this path, $E_m = 0.52$ eV, is so large that this mechanism is unlikely to contribute to the diffusion process. While the geometry of this path is similar to the other two **b** axis kick-out mechanisms, the hop distances for the first and last steps of the process are 0.2 Å longer. In addition, due to its proximity to the plane of Ge substitutions, the J interstitial site is the most stable of the interstitial

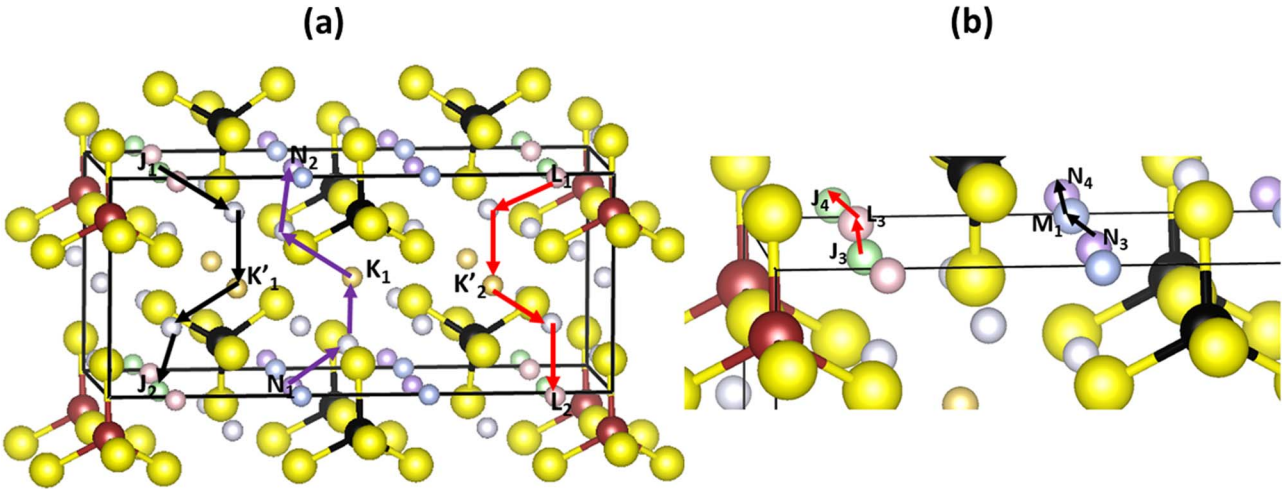

Figure 8. Ball and stick diagram of the $Li_{13/4}$ $As_{3/4}$ $Ge_{1/4}S_4$ using the same orientation and ball convention as Fig. 3a. (a) Shows three distinct migration paths with net motion along the **b** axis, involving interstitial ions and the "kick-out" of host lattice ions at each step, indicated with black, purple, and red arrows. (b) Shows two distinct migration paths with net motion along the **c** axis with pure interstitial processes, indicated with red and black arrows.

sites as shown in Table III. Both of these factors may explain the high migration energy of this path.

For the pure interstitial migration, two different paths with a net migration along the **c** axis were considered as shown in Fig. 8b. The migration energy was determined from the NEB calculations, as presented in Fig. 9b. These paths are similar to that found in pure Li_3AsS_4 where it involves the interstitial sites $I1_1 \rightarrow I1_2 \rightarrow I1_3$. For the path $J_3 \rightarrow L_3 \rightarrow J_4$, the first hop has a very low migration barrier apparently due to a correlated motion of the a^1 lattice site in a partial "kick-out" like process. For the second hop of this path, there is apparently no correlated motion by the nearby host Li ion of type a^2 and the overall migration barrier for this path is increased to $E_m = 0.42$ eV. The path $N_3 \rightarrow M_1 \rightarrow N_4$ involves the correlated motion of the nearby Li ion at a a^3 site on both hops, resulting in the overall migration energy for this path of $E_m = 0.29$ eV which is slightly lower than the corresponding migration energy of $E_m = 0.31$ eV in pure Li_3AsS_4.

Ion migration in $Li_{10/3}As_{2/3}Ge_{1/3}S_4$.—For the $Li_{10/3}As_{2/3}Ge_{1/3}S_4$ alloy, the lowest formation energy was found to be $E_f = 0.27$ eV, involving the B type interstitial and its neighboring x site vacancy, geometrically and energetically similar to the 1/4 alloy.

For modeling **b** axis migration with the kick-out mechanism, three different paths were considered, as shown in Fig. 10a. The corresponding minimum energy paths determined from NEB calculations are presented in Fig. 11a. The path sequence $A_1 \rightarrow a^2 \rightarrow K_1 \rightarrow b^2 \rightarrow A_2$ has a migration energy of $E_m = 0.23$ eV which is smaller than $E_m = 0.28$ eV and $E_m = 0.34$ eV for the corresponding migrations in the 1/4 alloy and pure Li_3AsS_4, respectively. The path sequence $C_1 \rightarrow a^2 \rightarrow K_2 \rightarrow b^3 \rightarrow C_2$ has a migration energy of $E_m = 0.30$ eV which very slightly smaller than $E_m = 0.31$ eV and $E_m = 0.34$ eV for the corresponding migrations in the 1/4 alloy and pure Li_3AsS_4, respectively. The third path considered in this study, $B_1 \rightarrow a^2 \rightarrow K_3 \rightarrow b^2 \rightarrow A_3$, has a relatively large migration barrier of $E_m = 0.39$ eV. The first hop of this path involves the B type interstitial site which tends to cause larger migration barriers due to its stability, similar behavior of the J site in the 1/4 alloy. The second hop of this process is identical (within the calculational error) to the $K_1 \rightarrow b^2 \rightarrow A_2$ sequence.

For the pure interstitial mechanism along the **c** axis, two paths were considered as shown in Fig. 10b with the corresponding NEB energy paths shown in Fig. 11b. The path $A_1 \rightarrow B_2 \rightarrow A_4$ has a migration energy of $E_m = 0.47$ eV. As in the case of the 1/4 alloy, the migration energy is large for this case due to the asymmetric correlated motion of nearby Li ions at inequivalent a sites. For the path $C_1 \rightarrow C_2 \rightarrow C_3$ the migration energy is $E_m = 0.2$ eV. As in the similar paths in the 1/4 alloy and the pure Li_3AsS_4, the migration involves the correlated partial kick-out of the neighboring Li ion at a a^2 site. In

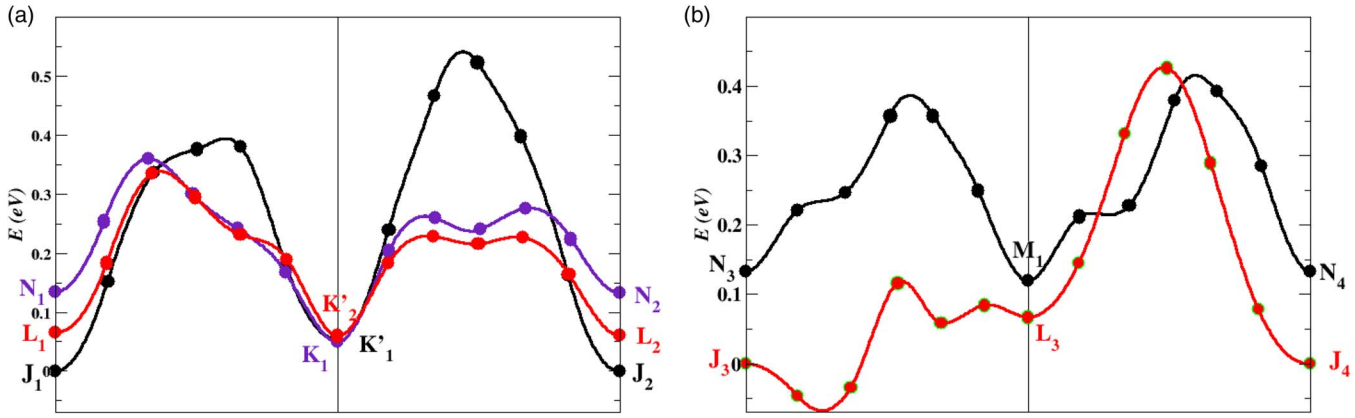

Figure 9. (a) Minimum energy paths as determined from the NEB method for the three distinct kick-out mechanism paths along the **b** axis shown in Fig. 8a. The line colors of the plot are consistent the arrows in the structural diagram. (b) Minimum energy paths as determined by the NEB method for the pure interstitial mechanism along the **c** axis corresponding to the diagram in Fig. 8b. The line colors of the plot are consistent the arrows in the structural diagram.

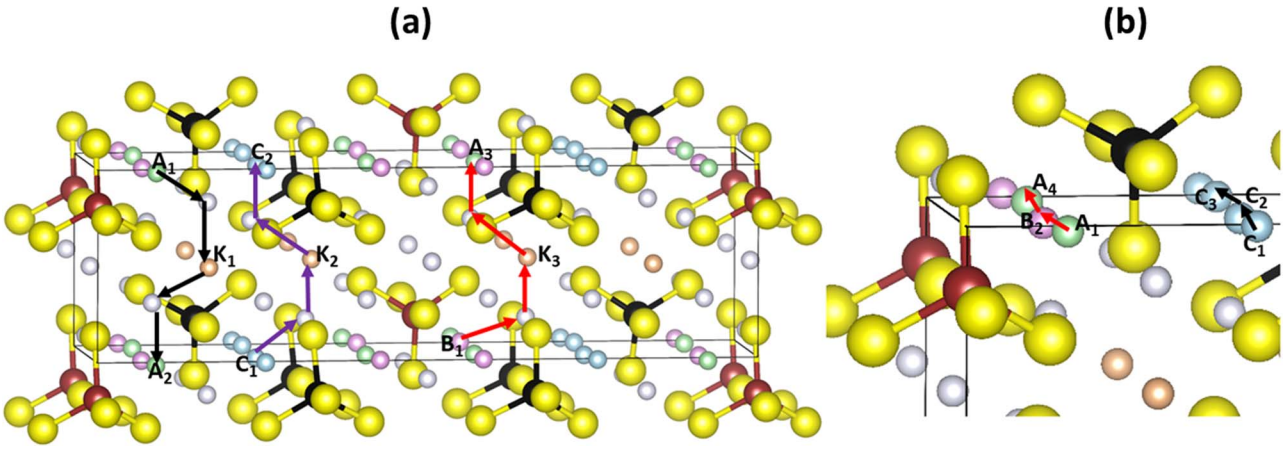

Figure 10. Ball and stick diagram of the $Li_{10/3}As_{2/3}Ge_{1/3}S_4$ using the same orientation and ball convention as Fig. 3b. (a) Shows migration paths with net motion along the **b** axis, with a process including the "kick-out" of host lattice ions at each step, indicated with black, purple, and red arrows. (b) Shows migration paths with net motion along the **c** axis with a pure interstitial process, indicated with red and black arrows.

this case, the resulting process has the lowest migration energy in the study.

Conclusions

As a result of this computational study, we are reasonably confident in our determination that pure Li_3AsS_4 forms in the $Pmn2_1$ crystal structure. Our first principles optimizations found this structure to have the lowest energy of those that we studied, and the results are in good agreement with the X-ray diffraction data reported by Sahu et al.,[3] as shown in Fig. 2.

The X-ray data of Sahu et al.[3] for the prepared materials with compositions $Li_{3+x}As_{1-x}Ge_xS_4$ suggests that they are substitutional alloys based on the Li_3AsS_4 structure. Our simulations assumed this to be the case, and the results are consistent. Despite the chemical similarities, the $Li_{3+x}As_{1-x}Ge_xS_4$ alloy system based on substitutions into the $Pmn2_1$ structure, is quite different from $Li_{3+x}P_{1-x}Ge_xS_4$ which has been shown[7] to undergo several structural transitions within a similar composition range. Presumably, the size similarity of the AsS_4 and GeS_4 building blocks help stabilize the $Pmn2_1$ structure.

We determined idealized models for the $x = 1/4$ and $x = 1/3$ alloys which turned out to be based on $2 \times 1 \times 1$ and $3 \times 1 \times 1$ supercells of Li_3AsS_4, respectively. The analysis shows how the $Pmn2_1$ structure can accommodate efficient ionic transport with a combination of interstitial and host lattice sites. For Li_3AsS_4 and the two alloy models, the migration of interstitial Li ions along the **c** axis gives the smallest value of the migration energy E_m. The migration of interstitial Li ions along the **b** axis using a kick-out process also gives a small value for E_m. The summary of the calculated values for the migration energies E_m as well as the energy E_f to form vacancy-interstitial pairs are given in Table VI where they are compared with the experimentally determined activation energies E_A. In general, we find $E_m \approx E_A$, suggesting that the prepared materials correspond to the "extrinsic" case described by Eq. 4. The simulations generally show that an important effect of Ge is to adjust the energies of the participating interstitial and vacancy Li ion sites to reduce E_m. Another effect of Ge is to stabilize an extra Li ion in the lattice at what we called the "x" site. Undoubtedly, this extra Li contributes to population of mobile interstitial Li ions, although our models cannot explain the details of these processes. The results of our simulations are in general agreement with the trends presented by the experimental work of Sahu et al.[3] One question that has not yet been resolved is the suggestion that the concentration $x = 1/3$ may be optimal. Our models show that the minimal values of the migration energies follow the trend $E_m(x = 0) > E_m(x = 1/4) > E_m(x = 1/3)$, suggesting that the substitional Ge incrementally reduces the migration barrier and improves the ionic conductivity.

The $Li_{3+x}As_{1-x}Ge_xS_4$ alloy system of Li ion conductors is the only system (that we know about) which is based on the $Pmn2_1$ structure. Several related alloy systems, such as $Li_{3+x}P_{1-x}Si_xS_4$

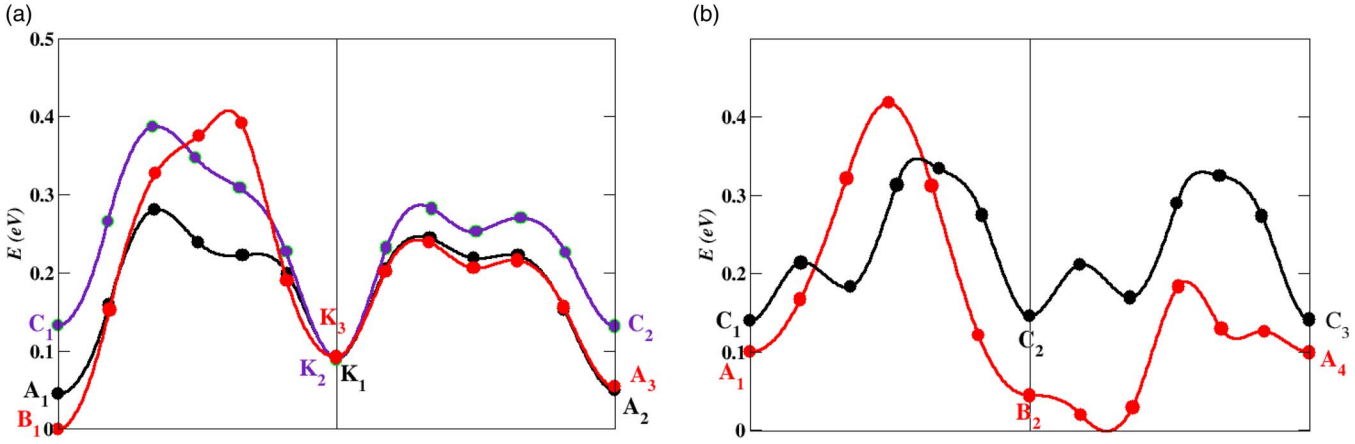

Figure 11. (a) Minimum energy paths as determined from the NEB method for the kick-out mechanism along the **b** axis corresponding to the diagram in Fig. 10a. The line colors correlate with the arrows in the structural diagram. (b) Minimum energy path as determined by the NEB method for the pure interstitial mechanism along the **c** axis corresponding to the diagram in Fig. 10b. The line colors correlate with the arrows in the structural diagram.

and $Li_{3+x}P_{1-x}Ge_xS_4$, transform into a *Pnma* structure or more complicated structures in order to achieve their improved Li ion conduction.[5,7]

Acknowledgments

This work was supported by NSF grants DMR-1105485 and DMR-1507942. Computations were performed on the Wake Forest University DEAC cluster, a centrally managed resource with support provided in part by the University. Help from Chaochao Dun and Ching-Wan Yip with digitizing the experimental X-ray results is gratefully acknowledged.

Appendix: Structural Details

This appendix lists the detailed structural parameters determined from the simulations. It is our experience that the fractional coordinates are generally in excellent agreement with experiment. The lattice constants, when scaled by a factor of 1.02 to compensate the systematic error of LDA, are also in excellent agreement with experiment. Table AI lists the fractional coordinates of Li_3AsS_4 in comparison with the corresponding coordinates of Li_3PS_4, showing the close similarity. Tables AII and AIII list the fractional coordinates of our models of the 1/4 and 1/3 alloys.

Table AI. Fractional coordinates of unique sites of the optimal structure of Li_3AsS_4 having the $Pmn2_1$ structure (with computed lattice constants $a = 7.57$ Å, $b = 6.54$ Å, $c = 6.13$ Å) in comparison with the corresponding coordinates for γ-Li_3PS_4 (with computed lattice constants $a = 7.55$ Å, $b = 6.45$ Å, $c = 6.05$ Å. The "Site" column lists the site multiplicity in the unit cell and the Wyckoff label.

Atom	Site	Li_3AsS_4 (x, y, z)	Li_3PS_4 (x, y, z)
Li	4b	(0.243, 0.319,−0.001)	(0.243, 0.317, 0.000)
Li	2a	(0.000, 0.152, 0.487)	(0.000, 0.150, 0.488)
As/P	2a	(0.000, 0.821, 1.000)	(0.000, 0.819, 0.999)
S	4b	(0.231, 0.666, 0.884)	(0.221, 0.670, 0.888)
S	2a	(0.000, 0.131, 0.879)	(0.000, 0.118, 0.886)
S	2a	(0.000, 0.813, 0.352)	(0.000, 0.811, 0.337)

Table AII. Fractional coordinates of unique sites of the optimal structure of $Li_{13/4}As_{3/4}Ge_{1/4}S_4$ (with computed lattice constants $a = 15.20$ Å, $b = 6.60$ Å, and $c = 6.13$ Å) The multiplicity of the site within the simulations cell and the Li labels as defined in Fig. 3a (rather than the labels of its Pm space group) are also listed.

Atom	Mult.	Label	(x, y, z)
Li	1	a^1	(0.000, 0.107, 0.510)
Li	2	b^1	(±0.138, 0.691, 0.514)
Li	2	a^2	(±0.247, 0.840, 0.026)
Li	2	b^2	(±0.122, 0.319, 0.994)
Li	1	a^3	(0.500, 0.164, 0.516)
Li	2	b^3	(±0.372, 0.692, 0.495)
Li	2	b^4	(±0.379, 0.318, 0.997)
Li	1	x	(0.000, 0.483, 0.341)
As	1		(0.500, 0.822, 0.998)
As	2		(±0.249, 0.186, 0.496)
Ge	1		(0.000, 0.818, 0.001)
S	1		(0.000, 0.135, 0.115)
S	1		(0.500, 0.127, 0.123)
S	1		(0.000, 0.782, 0.641)
S	1		(0.500, 0.825, 0.646)
S	2		(±0.116, 0.655, 0.131)
S	2		(±0.616, 0.664, 0.110)
S	2		(±0.129, 0.335, 0.607)
S	2		(±0.637, 0.350, 0.611)
S	2		(±0.254, 0.886, 0.634)
S	2		(±0.250, 0.179, 0.144)

Table AIII. Fractional coordinates of unique sites of the optimal structure with space group $Pmn2_1$ of $Li_{10/3}As_{2/3}Ge_{1/3}S_4$ (with computed lattice constants $a = 22.77$ Å, $b = 6.60$ Å, and $c = 6.14$ Å) The multiplicity of the site within the simulations cell and Wyckoff label, as well as the Li labels as defined in Fig. 3b are also listed.

Atom	Mult.	Label	(x, y, z)
Li	2 a	x	(0.000, 0.474, 0.664)
Li	2 a	a^1	(0.000, 0.098, 0.496)
Li	4 b	b^1	(0.092, 0.683, 0.489)
Li	4 b	a^2	(0.167, 0.827, 0.972)
Li	4 b	b^2	(0.082, 0.311, 0.010)
Li	4 b	b^3	(0.251, 0.311, 0.002)
As	4 b		(0.335, 0.822, 0.003)
Ge	2 a		(0.000, 0.810, 0.002)
S	2 a		(0.000, 0.128, 0.890)
S	2 a		(0.000, 0.774, 0.361)
S	4 b		(0.740, 0.653, 0.884)
S	4 b		(0.078, 0.647, 0.871)
S	4 b		(0.415, 0.673, 0.897)
S	4 b		(0.669, 0.122, 0.865)
S	4 b		(0.833, 0.167, 0.853)

References

1. Y. Wang, W. D. Richards, S. P. Ong, L. J. Miara, J. C. Kim, Y. Mo, and G. Ceder, *Nature Materials*, **14**, 1026 (2015).
2. J. Li, C. Ma, M. Chi, C. Liang, and N. J. Dudney, *Advanced Energy Materials*, **5**, 1041408 (2015).
3. G. Sahu, E. Rangasamy, J. Li, Y. Chen, K. An, N. Dudney, and C. Liang, *Journal of Materials Chemistry A*, **2**, 10396 (2014).
4. Y.-W. Hu, I. D. Raistrick, and R. A. Huggins, *Journal of the Electrochemical Society*, **124**, 1240 (1977).
5. H. Deng, P. Nie, H. Luo, Y. Zhang, J. Wang, and X. Zhang, *J. Mater. Chem. A*, **2**, 18256 (2014).
6. T. Hahn, ed., *International Tables for Crystallography, Volume A: Space-group symmetry, Fifth revised edition* (Kluwer, 2002) ISBN 0-7923-6590-9.
7. S. Hori, M. Kato, K. Suzuki, M. Hirayama, Y. Kato, and R. Kanno, *Journal of the American Ceramic Society*, **98**, 3352 (2015).
8. K. Homma, M. Yonemura, T. Kobayashi, M. Nagao, M. Hirayama, and R. Kanno, *Solid State Ionics*, **182**, 53 (2011).
9. N. Kamaya, K. Homma, Y. Yamakawa, M. Hirayama, R. Kanno, M. Yonemura, T. Kamiyama, Y. Kato, S. Hama, K. Kawamoto, and A. Mitsui, *Nature Materials*, **10**, 682 (2011).
10. R. Kanno and M. Murayama, *Journal of the Electrochemical Society*, **148**, A742 (2001).
11. Z. Liu, W. Fu, E. A. Payzant, X. Yu, Z. Wu, N. J. Dudney, J. Kiggans, K. Hong, A. J. Rondinone, and C. Liang, *Journal of the American Chemical Society*, **135**, 975 (2013).
12. M. Tachez, J.-P. Malugani, R. Mercier, and G. Robert, *Solid State Ionics*, **14**, 181 (1984).
13. P. Hohenberg and W. Kohn, *Physical Review*, **136**, B864 (1964).
14. W. Kohn and L. J. Sham, *Physical Review*, **140**, A1133 (1965).
15. P. E. Blöchl, *Phys. Rev. B*, **50**, 17953 (1994).
16. N. A. W. Holzwarth, A. R. Tackett, and G. E. Matthews, *Computer Physics Communications*, **135**, 329 (2001), available from the website http://pwpaw.wfu.edu.
17. P. Giannozzi, S. Baroni, N. Bonini, M. Calandra, R. Car, C. Cavazzoni, D. Ceresoli, G. L. Chiarotti, M. Cococcioni, I. Dabo, A. D. Corso, S. de Gironcoli, S. Fabris, G. Fratesi, R. Gebauer, U. Gerstmann, C. Gougoussis, A. Kokalj, M. Lazzeri, L. Martin-Samos, N. Marzari, F. Mauri, R. Mazzarello, S. Paolini, A. Pasquarello, L. Paulatto, C. Sbraccia, S. Scandolo, G. Sclauzero, A. P. Seitsonen, A. Smogunov, P. Umari, and R. M. Wentzcovitch, *J. Phys.: Condens. Matter*, **21**, 394402 (2009), available from the website http://www.quantum-espresso.org.
18. A. Kokalj, *Journal of Molecular Graphics and Modelling*, **17**, 176 (1999), code available at the website http://www.xcrysden.org.
19. A. Kokalj, *Computational Materials Science*, **28**, 155 (2003).
20. K. Momma and F. Izumi, *Applied Crystallography*, **44**, 1272 (2011), code available from the website http://jp-minerals.org/vesta/en/.
21. J. P. Perdew and Y. Wang, *Phys. Rev. B*, **45**, 13244 (1992).
22. Y. A. Du and N. A. W. Holzwarth, *Phys. Rev. B*, **76**, 174302 (2007).
23. N. A. W. Holzwarth, N. D. Lepley, and Y. A. Du, *Journal of Power Sources*, **196**, 6870 (2011).
24. Y. A. Du and N. A. W. Holzwarth, *Phys. Rev. B*, **81**, 184106 (2010).
25. N. D. Lepley and N. A. W. Holzwarth, *Journal of the Electrochemical Society*, **159**, A538 (2012).
26. N. D. Lepley, N. A. W. Holzwarth, and Y. A. Du, *Phys. Rev. B*, **88**, 104103 (2013).

27. K. Senevirathne, C. S. Day, M. D. Gross, A. Lachgar, and N. A. W. Holzwarth, *Solid State Ionics*, **333**, 95 (2013).
28. N. D. Lepley and N. A. W. Holzwarth, *Phys. Rev. B*, **92**, 214201 (2015).
29. Z. D. Hood, C. Kates, M. Kirkham, S. Adhikari, C. Liang, and N. A. W. Holzwarth, *Solid State Ionics*, **284**, 61 (2015).
30. L. E. Rush Jr. and N. A. W. Holzwarth, *Solid State Ionics*, **286**, 45 (2016).
31. W. M. Haynes, ed., *CRC Handbook of Chemistry and Physics*, 92th Edition (CRC Press, Taylor & Francis Group, 2011) ISBN 978-1-4398-5511-9.
32. A. Van De Walle and G. Ceder, *Reviews of Modern Physics*, **74**, 11 (2002).
33. H. Jónsson, G. Mills, and K. W. Jacobsen, in *Classical and Quantum Dynamics in Condensed Phase Simulations*, edited by B. J. Berne, G. Ciccotti, and D. F. Coker (World Scientific, Singapore, 1998) pp. 385–404.
34. G. Henkelman, B. P. Uberuaga, and H. Jónsson, *J. Chem. Phys.*, **113**, 9901 (2000).
35. G. Henkelman and H. Jónsson, *J. Chem. Phys.*, **113**, 9978 (2000).
36. A. R. West, *Basic Solid State Chemistry*, second edition (John Wiley & Sons, LTD, 1999).
37. G. Makov and M. C. Payne, *Physical Review B*, **51**, 4014 (1995).
38. C. Freysoldt, J. Neugebauer, and C. G. Van de Walle, *Physical Review Letters*, **102** (2009).
39. P. Ganesh, A. A. Lubimtsev, G. K. P. Dathar, J. Anchell, P. R. C. Kent, A. J. Rondinone, and B. G. Sumpter, *Bulletin of the American Physical Society*, **60** (2015), APS March Meeting 2015.
40. Z. Liu, W. Fu, E. A. Payzant, X. Yu, Z. Wu, N. J. Dudney, J. Kiggans, K. Hong, A. J. Rondinone, and C. Liang, *Journal of the American Chemical Society*, **135**, 975 (2013).
41. K. Homma, M. Yonemura, T. Kobayashi, M. Nago, M. Hirayama, and R. Kanno, *Solid State Ionics*, **182**, 53 (2011).
42. R. Mercier, J.-P. Malugani, B. Fahys, and G. Robert, *Acta Cryst.*, **B38**, 1887 (1982).
43. "Mercury 3.5.1", (2014), developed and distributed by the Cambridge Crystallographic Data Centre http://www.ccdc.cam.ac.uk/mercury/.
44. G. Sahu, Z. Lin, J. Li, Z. Liu, N. Dudney, and C. Liang, *Energy Environ. Sci.*, **7**, 1053 (2014).
45. Y. Matsushita and M. G. Kanatzidis, *Z. Naturforsch.*, **53 b**, 23 (1998).
46. M. Murayama, R. Kanno, Y. Kawamoto, and T. Kamiyama, *Solid State Ionics*, **154–155**, 789 (2002).
47. J. H. MacNeil, D. M. Massi, J.-H. Zhang, K. A. Rosmus, C. D. Brunetta, T. A. Gentile, and J. A. Aitken, *Journal of Alloys and Compounds*, **586**, 736 (2014).
48. R. Grau-Crespo, S. Hamad, C. R. A. Catlow, and N. H. d. Leeuw, *Journal of Physics: Condensed Matter*, **19**, 256201 (2007).